



Photocatalytic preparation of nanostructured MnO_2 –(Co_3O_4)/ TiO_2 hybrids: The formation mechanism and catalytic application in SCR de NO_x reaction



Lei Huang ^{a,*}, Xiaonan Hu ^a, Shuai Yuan ^a, Hongrui Li ^a, Tingting Yan ^a, Liyi Shi ^b, Dengsong Zhang ^{a,*}

^a Research Center of Nano Science and Technology, Shanghai University, Shanghai 200444, PR China

^b Department of Chemistry, Shanghai University, Shanghai 200444, PR China

ARTICLE INFO

Article history:

Received 22 June 2016

Received in revised form 22 October 2016

Accepted 26 October 2016

Available online 27 October 2016

Keywords:

Photocatalysis

MnO_2 –(Co_3O_4)/ TiO_2

Nanostructure

TiO_2

De NO_x

ABSTRACT

Photocatalysis has already triggered enormous researches in the areas of solar energy transfer, environmental purification, organic synthesis and etc. In this work, the photocatalytic reactions were applied to controllably prepare nanostructured MnO_2 –(Co_3O_4)/ TiO_2 hybrids with highly distributed active components. The loading of flocculent MnO_2 over TiO_2 nanorods was rapidly achieved through the redox reactions between the MnO_4^- and photoexcited electrons. Three steps were involved in the formation of MnO_2 – Co_3O_4 hybrids, namely the oxidation of Co^{2+} to Co^{3+} by the photogenerated holes, the deposition of intermediate CoOOH over MnO_2 and finally the decomposition of CoOOH by calcination to form Co_3O_4 . Selective catalytic reduction of NO with NH_3 (NH_3 -SCR) has been chosen as a model reaction to explore its application. It was found out that the unique MnO_2 –(Co_3O_4)/ TiO_2 hybrids exhibited promoted low temperature performance compared to that of prepared via impregnation, which was attributed to the abundant MnO_2 species, surface active oxygen, surface Ti^{3+} species and acid sites. We believe the MnO_2 –(Co_3O_4)/ TiO_2 hybrids were also interested in other applications of environmental catalysis.

© 2016 Elsevier B.V. All rights reserved.

1. Introduction

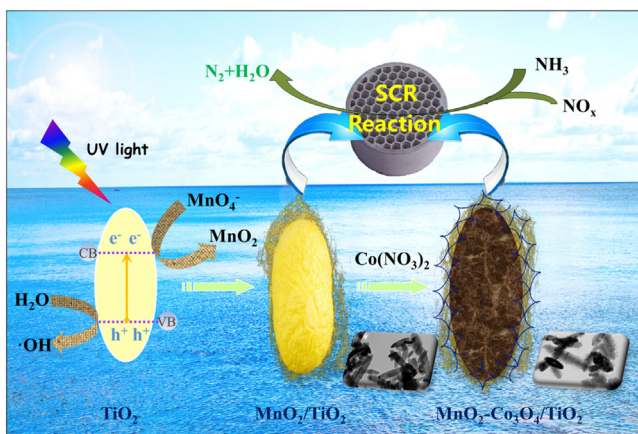
Photocatalysis has already triggered enormous researches in the areas of solar energy transfer and environmental purification [1–3] since the discovery of hydrogen evolution through electrochemical photolysis of H_2O on TiO_2 by Fujishima and Honda in 1972 [4]. The principle of photocatalysis over semiconductors is to utilize the photogenerated electrons and holes which could migrate to the surface to produce corresponding reduction and oxidation reactions [5,6]. The most important photocatalytic reduction reactions are the reduction of H_2O or CO_2 to produce H_2 or hydrocarbon for the transfer of solar energy to chemical energy or chemical products [7,8]. The most studied oxidation reactions are the oxidation and mineralization of organic compounds for environmental remediation [9,10]. Recent great progress about the utilization of photocatalytic reaction is in the field of organic synthesis [11–13].

Therefore, the exploration of photocatalytic reactions in different applications is interesting and meaningful.

In the past several decades, the photocatalytic process has also been used to in-situ deposit noble metals (Pt, Au, Ag, Pd, Ni and etc.) in the form of nanoparticles as reduction co-catalyst to promote the separation of photo-induced carriers, which is favorable to the followed chemical reactions [14–16]. On the other hand, oxides (MnO_x , CoO_x , PbO_2 and etc.) nanostructures were also reported to be photocatalytically loaded over the semiconductors as oxidation co-catalyst to accelerate the oxidation reaction, especially in the oxidation of water [17,18]. Both cases have forcefully demonstrated that the photocatalytic reactions could be utilized to load metals and metal oxides over the photocatalysts for fabricating functional materials. However, seldom researches focused on the morphologies and the components of the co-catalysts and their further application in other catalytic reactions beyond the photocatalytic reactions. Interestingly, we noticed that the common photocatalysts, such as TiO_2 , ZnO_2 , CeO_2 and etc., are also frequently used as supports in selective catalytic reduction (SCR), CO oxidation, the oxidation of formaldehyde and many other catalytic reactions [19,20]. Furthermore, the cocatalysts like MnO_x and CoO_x in photocatalytic fields [21] are also important active compo-

* Corresponding authors.

E-mail addresses: leihuang@shu.edu.cn (L. Huang), dszhang@shu.edu.cn (D. Zhang).



Scheme 1. The formation procedures of MnO₂-(Co₃O₄)/TiO₂ hybrids and their catalytic application in SCR deNO_x reaction.

nents in above catalytic reactions [22,23]. It is therefore expected that the catalysts containing both support and active components employed in other catalytic reactions might be achieved via the green and sustainable photocatalytic reactions.

SCR of NO_x with NH₃ is considered as the state-of-the-art technique for the abatement of NO_x which would profoundly endanger human health and environmental sustainability [24]. The most challenging and urgent demand is to develop highly efficient SCR catalysts worked at low temperature (below 200 °C) [25]. Among these high efficient low temperature alternative materials, manganese based catalysts have attracted enormous research interest due to the outstanding redox properties [26]. Recently, great efforts have been devoted to integrate manganese oxides with cobalt oxides on the supports which deliver superior SCR performance at low temperature [27]. In this regard, it is highly desirable to fabricate Mn based or Mn-Co compounds with highly distribution and specific morphologies on the supports.

Herein, we successfully demonstrated the feasibility to fabricate nanostructured MnO₂-(Co₃O₄)/TiO₂ hybrids as SCR catalyst via the environmentally benign photocatalytic reactions. The synthesis strategy is schematically illustrated in Scheme 1. TiO₂ nanorods (NRs) were chosen as the support for photocatalytically loading active components. Flocculent MnO₂ sheets could be easily obtained and closely anchored on the TiO₂ NR through the photocatalytic reduction of KMnO₄ in the irradiation of UV light. By using a similar procedure, Co could be further introduced and equally distributed in the MnO₂ sheets around the TiO₂ NR. The morphologies, crystallographic structures and surface properties were thoroughly investigated by Field Emission Transmission Electron Microscope (FETEM), High resolution transmission electron microscopic (HRTEM), X-ray powder diffraction (XRD) and X-ray photoelectron spectroscopy (XPS). The formation mechanism of MnO₂/TiO₂ and MnO₂-Co₃O₄/TiO₂ nanostructures was systematically studied. The MnO₂-(Co₃O₄)/TiO₂ hybrids were further evaluated as the catalyst for the SCR of NO_x by NH₃. It was found that both the MnO₂/TiO₂ and MnO₂-Co₃O₄/TiO₂ exhibited promoted SCR activities at low temperature compared with that of MnO₂/TiO₂ prepared by impregnation method.

2. Experiment

2.1. Synthesis of TiO₂ nanorods

All chemical reagents, which were purchased commercially from Sinopharm Chemical Reagent Company, were of analytical grade and used as received without further purification.

TiO₂ NRs were synthesized from Degussa P25 via a two-step hydrothermal recrystallization treatment as previously reported by Xu and coworkers [28]. Briefly, 2.0 g of P25 and 32 g of NaOH were dissolved in 40 mL of deionized water, respectively. After shaking gently by hand for about 2 min, the above solutions were mixed intensively and then transferred into a 100 mL Teflon-lined stainless steel autoclave, which was then kept in an electric oven at 120 °C for 24 h. After cooling naturally to room temperature, the product was washed with deionized water several times until the pH of the solution was about 10.5. Subsequently, the Na-titanates were collected by centrifugation at the speed of 13,000 r/min for 5 min. 2.0 g of the above wet Na-titanates product was then dispersed in 80 mL of deionized water by ultrasonication. The obtained uniform suspension was then transferred into a 100 mL Teflon-lined stainless steel autoclave and kept at 200 °C for 24 h. After taken out from the oven to cool down to room temperature, the precipitate was isolated by several rinse-filtration cycles. Finally, the samples were dried in vacuum at 60 °C overnight and then calcinated at 400 °C for 2 h to next-step usage.

2.2. Preparation of MnO₂ decorated TiO₂ nanorods and MnO₂-Co₃O₄ decorated TiO₂ nanorods heterostructures

The MnO₂ nanostructures were supported on TiO₂ NRs to prepare novel Mn/TiO₂ materials employing photocatalytic reactions. In a typical preparation process, 0.1 g of TiO₂ NRs as support materials were ultrasonically dispersed in 160 mL of deionized water to obtain a homogeneous milk-like suspension. Afterwards, 40 mL 0.040 g of KMnO₄ solution was added in the above suspension. After vigorously stirring for 10 min, the reaction mixture was subjected to irradiate in the UV section of 300 W Xe lamp (PLS-SXE300C) under constant magnetic stirring, followed by reacting for 2 h with a circulating cooling water system to keep the whole reaction process at 20 °C. The resulting products were harvested by filtration and washed thoroughly with deionized water. Finally, the material was freeze-dried for 20 h and then loaded into a tube furnace to anneal under air atmosphere at 350 °C for 2 h at a ramping rate of 1 °C min⁻¹ to obtain the products with a TiO₂ core wrapped up by a flocculent MnO₂ shell. The as-obtained materials were denoted by Mn/TiO₂-P, where P represented the method of photocatalytic reactions.

The synthesis of MnO₂-Co₃O₄ supported TiO₂ NRs ternary composites were based on a similar procedure to the preparation of Mn/TiO₂-P with exception that the addition of 5 mL 0.218 g Co(No₃)₂·6H₂O for another 2 h in the UV irradiation while keeping other conditions identical. In other words, the sample was obtained in KMnO₄ solution for 2 h of irradiation in the first step and in KMnO₄ and Co(No₃)₂·6H₂O hybrid solution for continually 2 h of irradiation in the second step. The obtained sample was designated as Mn-Co/TiO₂-P. Co/TiO₂-P as a blank control trial was obtained by using 2.180 g Co(No₃)₂·6H₂O and 0.246 g NaO₃ without KMnO₄ under UV light.

For comparison, Mn/TiO₂ (the Mn loading was designed as 2 wt.% depending on the amounts via photocatalytic reactions) was prepared by an incipient wetness impregnation method using TiO₂ NRs as support material and Mn(CH₃COO)₂·4H₂O as precursor salts. The heat treatment was performed in air at 500 °C for 2 h with a temperature ramp of 2 °C min⁻¹. The as-obtained sample was denoted as Mn/TiO₂-I. Besides, Mn-Co/TiO₂ (the Mn or Co loading was both designed as 4 wt.% depending on the amounts via photocatalytic reactions) was also prepared by an incipient wetness impregnation method using TiO₂ NRs as support material and Mn(CH₃COO)₂·4H₂O and Co(No₃)₂·6H₂O as precursor salts. The heat treatment was performed in air at 500 °C for 2 h with a tem-

perature ramp of $2\text{ }^{\circ}\text{C min}^{-1}$. The as-obtained sample was denoted as Mn-Co/TiO₂-I.

2.3. Characterization

The morphologies and microstructures, as well as elemental distribution, were examined with transmission electron microscopic (TEM, JEM-200CX) and Field Emission Transmission Electron Microscope (FETEM, Tecnai G2 F20 S-Twin). The chemical composition and crystallographic structure of all as-synthesized samples was analyzed with X-ray powder diffraction (XRD) on a Rigaku D/MAX2200 VPC equipped with a Cu K α radiation operated at 40 kV and 40 mA and a secondary beam graphite monochromator from $10\text{ }^{\circ}\text{C}$ to $90\text{ }^{\circ}\text{C}$ at a scan rate of $8\text{ }^{\circ}\text{C min}^{-1}$. N₂ adsorption–desorption isotherms were obtained at 77 K on a Quantachrome instrument (Autosorb IQ2-2MP-C). Prior to each measurement, the samples (ca. 100 mg) were degassed at $300\text{ }^{\circ}\text{C}$ under N₂ atmosphere for 4 h. The specific surface areas, the pore volumes and average pore diameters were measured using the Brunauer–Emmett–Teller (BET) equation and the Barrett–Joyner–Halenda (BJH) method from the desorption branches of the isotherms.

The ultraviolet-visible absorption spectra were recorded on a double beam UV–vis spectrophotometer (UV-2600, Shimadzu, Japan). The thermal behavior of the as-prepared sample was conducted by thermogravimetric analysis and differential scanning calorimetry analysis (TGA and DSC, Netzsch STA449F3) at a heating rate of $10\text{ }^{\circ}\text{C min}^{-1}$ from room temperature to $800\text{ }^{\circ}\text{C}$ in a dynamic atmosphere of air. The chemical composition and contents of the samples were measured by Perkin Elmer 7300DV inductive coupled plasma atomic emission spectrometry (ICP-AES). The X-ray photo-electron spectroscopy (XPS) were carried out on an RBD upgraded PHI-5000C ESCA system, using Mg K α radiation as the excitation source. All of the binding energy (BE) spectra were calibrated with the C 1s line centered at 284.6 eV from contaminant carbon. Curve fitting and background subtraction were accomplished employing AugerScan 3.21 software.

The temperature-programmed reduction with H₂ (H₂-TPR) or desorption with NH₃ (NH₃-TPD) experiments were all performed on a Tianjin XQ TP5080 autoadsorption apparatus. Before each experiment, the samples (150 mg) were placed in a quartz tube with quartz wool and pre-treated at $300\text{ }^{\circ}\text{C}$ for 30 min at a ramping rate of $10\text{ }^{\circ}\text{C min}^{-1}$ under a constant high-purity N₂ (for H₂-TPR) or He (for NH₃-TPD) flow rate of 30 mL/min, respectively. For H₂-TPR, after cooling down to room temperature in the N₂ atmosphere, the flowing gas was adjusted to the mixture gas of H₂ (10 vol.%)/N₂ (30 mL/min) and the samples were raised to $800\text{ }^{\circ}\text{C}$ at a constant heating rate of $10\text{ }^{\circ}\text{C min}^{-1}$. As for NH₃-TPD, the samples were switched to a flow of NH₃ (500 ppm) for 1 h to adsorb NH₃ at $100\text{ }^{\circ}\text{C}$, followed by He flushing for 0.5 h to remove physisorbed NH₃. During the desorption process, the samples were heated to $800\text{ }^{\circ}\text{C}$ with a temperature ramp of $10\text{ }^{\circ}\text{C min}^{-1}$ under a flow of He (30 mL/min).

In situ diffuse reflectance infrared Fourier transform spectroscopy (In situ DRIFTS) experiments were conducted by accumulating 64 scans at a 4 cm^{-1} resolution in the kubelka-Munk format from 2000 to 800 cm^{-1} on an FTIR spectrometer (Nicolet 6700) equipped with a Harrick Scientific DRIFT cell and a mercury-cadmium-telluride MCT/A detector. Prior to each experiment, the catalysts were pretreated at $350\text{ }^{\circ}\text{C}$ in a flow of N₂ (50 mL/min) for 0.5 h to remove physisorbed water and then cooled to target temperature under N₂ flow to obtain a background spectra and the spectrum was automatically subtracted from the corresponding spectra. The FT-IR spectra were recorded after pyridine adsorption by a Bruker Vector 27 spectrometer (Py-IR). The sample (~ 20 mg) was compacted to a wafer and heated at $400\text{ }^{\circ}\text{C}$ for 1 h in an IR gas cell before adsorption of pyridine under high vacuum. Then

the samples were calcined at $100\text{ }^{\circ}\text{C}$ after pyridine adsorption at room temperature, followed by stepwise heating to illustrate the strength and types of the acid sites.

2.4. Catalytic performance tests

The reduction reaction of NO by NH₃ was performed on a fixed-bed reactor consisting of a vertical stainless steel tube with an internal diameter of 8 mm enclosed in a temperature-controlled furnace. The test system was operated with a 250 mL/min of total flow rate, which is composed by 500 ppm of NO, 500 ppm of NH₃, 5 vol.% of O₂, 8 vol.% of H₂O (when used) and N₂ as balance in inlet with a gas hourly space velocity (GHSV) of $30,000\text{ h}^{-1}$. The catalysts were crushed and sieved to collect the mesh fraction (0.4 g, 20–40 mesh). The concentration of the feed gases and the effluent streams were monitored on-line continuously by a Signal flue gas detector. All data were recorded at the chosen temperature from 90 to $350\text{ }^{\circ}\text{C}$ after steady state was achieved at each temperature step.

The NO conversion and N₂ selectivity were calculated using the equations below:

$$\text{NO conversion}(\%) = \frac{[\text{NO}]_{\text{in}} - [\text{NO}]_{\text{out}}}{[\text{NO}]_{\text{in}}} \times 100\%$$

$$\text{N}_2 \text{ selectivity} = \left(1 - \frac{2[\text{N}_2\text{O}]_{\text{out}}}{[\text{NO}_x]_{\text{in}} + [\text{NH}_3]_{\text{in}} - [\text{NO}_x]_{\text{out}} - [\text{NH}_3]_{\text{out}}} \right) \times 100\%$$

where the $[\text{NO}]_{\text{in}}$ and $[\text{NO}]_{\text{out}}$ denoted the inlet and outlet gas concentration of NO, respectively. $[\text{NO}_x]_{\text{in}}$ and $[\text{NO}_x]_{\text{out}}$ denoted the inlet and outlet gas concentration of both NO and NO_x, respectively. $[\text{N}_2\text{O}]_{\text{out}}$ denoted the outlet gas concentration of N₂O. $[\text{NH}_3]_{\text{in}}$ and $[\text{NH}_3]_{\text{out}}$ denoted the inlet and outlet gas concentration of NH₃, respectively.

3. Results and discussion

3.1. The characterization of the materials

The FETEM images of Mn/TiO₂-I, Mn/TiO₂-P and Mn-Co/TiO₂-P are shown in Fig. 1. Fig. 1a clearly reveals that monodisperse fine MnO_x nanoparticles with an average size of $\sim 2\text{ nm}$ were supported on TiO₂ nanorods. Very interestingly, the morphology of the MnO_x prepared via photocatalytic reaction over the scaffold of TiO₂ NRs is quite different. Fig. 1b displays that the MnO_x is in the form of flocculent structure composed by many flexible nanosheets and closely anchored on the backbone of TiO₂ NRs, indicating the successful deposition of nanostructured MnO_x via photocatalytic method. Furthermore, with the introduction of Co, the nanosheets structures become rougher and more stacked as appreciated in Fig. 1c. It is expected that the flexible, spatial and open nanostructure obtained via photocatalytic reaction would provide a large specific surface area. The N₂ adsorption–desorption isotherms of all the samples increased sharply in the high pressure range of $P/P_0 = 0.90\text{--}1.0$, suggesting the existence of mesoporous which are ascribed to the interparticles voids. In fact, the specific surface areas of Mn/TiO₂-P ($36.6\text{ m}^2\text{ g}^{-1}$) and Mn-Co/TiO₂-P ($35.1\text{ m}^2\text{ g}^{-1}$) are both larger than that of bare TiO₂ ($21.6\text{ m}^2\text{ g}^{-1}$) and Mn/TiO₂-I ($21.0\text{ m}^2\text{ g}^{-1}$), with the results shown in Table 1, which endowed abundant active sites for gas absorption resulting in an enhanced catalytic performance.

The distribution of MnO_x and Mn-Co components over TiO₂ were further observed by the EDX mapping. Fig. 1d–n indicate that both MnO_x and Mn-Co compounds were uniformly deposited on the out surface of TiO₂ NR and unambiguously confirms the hierarchical shell/core nanostructure of MnO_x-(CoO_x)/TiO₂. It

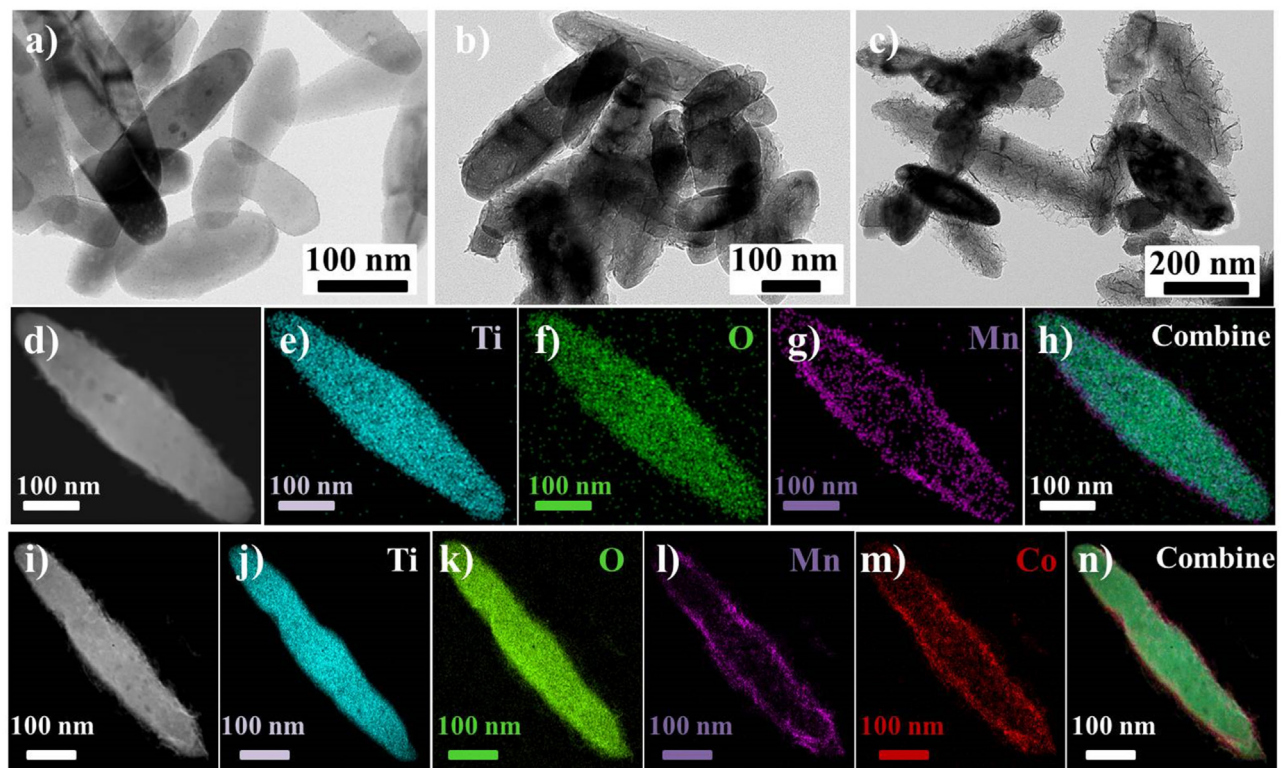


Fig. 1. Field-emission TEM images of the samples via different preparation processes.

(a, Mn/TiO₂-I; b, Mn/TiO₂-P; c, Mn-Co/TiO₂-P); The EDX mapping patterns of the Mn/TiO₂-P (d-h) and Mn-Co/TiO₂-P (i-n).

Table 1
The specific surface area and pore information of different samples.

Sample	Surface area (m ² g ⁻¹)	Pore size (nm)	Pore volume(cm ³ g ⁻¹)
TiO ₂ NR	21.6	1.94	0.29
Mn/TiO ₂ -I	21.0	2.19	0.26
Mn/TiO ₂ -P	36.6	2.18	0.25
Mn-Co/TiO ₂ -P	35.1	1.94	0.23

demonstrated that Mn and Co species could be uniformly deposited on the TiO₂ via photocatalytic method. The highly dispersed active species is suggested to be beneficial to the catalytic performance [29].

The crystallographic structures of the materials were determined by HRTEM and SAED analysis as depicted in Fig. 2 and S1. The inset in Fig. S1a confirmed the single-crystal structure of TiO₂ NR. As for Mn/TiO₂-I (Fig. 2a–b), the lattice spacing is calculated to be ca. 0.184 nm, which is ascribed to (431) plane of Mn₂O₃ (JCPDS No. 41-1442) and in good agreement with the previous reports via impregnation method [30]. Nevertheless, Mn/TiO₂-P shows visible distinct lattice fringes in Fig. 2c–d, where the interplanar distance is measured to be about 0.238 nm, corresponding to the (004) planar space of crystalline MnO₂ (JCPDS No. 44-0141). With respect to Mn-Co/TiO₂-P, both MnO₂ and Co₃O₄ lattice fringes (JCPDS No. 42-1467) after calcination can be clearly observed, in which the lattice spacing of Co₃O₄ were approximately 0.244 nm. These facts indicated that the photocatalytic method would give rise to different crystalline phase compared with traditional impregnation method.

The samples are subsequently characterized by powder XRD to identify its crystallographic structure (Fig. 3a), where all samples exhibit a similar profile and all the identified peaks can be unambiguously assigned to TiO₂ (anatase, JCPDS No. 21-1272). It suggested that the TiO₂ NRs after calcination were thermodynamically stable and had no crystalline transformation. No relational

Mn and/or Co crystalline formations and also other impurities or contaminants were detected which was probably due to the low content and/or highly dispersion of the Mn and/or Co species. To identify the MnO₂ crystallographic structures from XRD, we then prolonged the photocatalytic reaction duration up to 12 h to load MnO₂ (Fig. 3b). We indeed observed the appearance of a new peak at ca. 12.8° which was assigned to the (110) diffraction of MnO₂ (highlighted by navy rectangle in Fig. 3b). These observations further confirmed that the crystallographic structure achieved by photocatalytic method is in the form of highly distributed MnO₂, in keeping with the EDX mapping and HRTEM results.

The loading amounts of MnO₂ and/or Co₃O₄ were studied by ICP-AES and UV-vis DRS. Table S1 shows that Mn/TiO₂-I and Mn/TiO₂-P have close Mn percentage of 1.65% and 1.92%, respectively. However, the introduction of Co notably increased the Mn percentage to 3.38% which was probably due to the increased irradiation duration. Actually, we further proved that the decrease of irradiation duration to 60 min and 15 min caused the decrease of Mn percentage to 1.42% and 0.80%, as also shown in Table S1. The corresponding colors of these samples are also different (Fig. S2). The colors of Mn/TiO₂-I, Mn/TiO₂-P and Mn-Co/TiO₂-P were light green, earth yellow and dark green, respectively. This is consistent with UV-vis DRS results (Fig. S3). It was observed that pure TiO₂ NR is not sensitive in the visible region (above 400 nm), while Mn/TiO₂ and Mn-Co/TiO₂ displayed a very broad absorption band in the range of 400–800 nm. In addition, the absorption in the visible range increased with the increasing irradiation durations. This further demonstrated the loading amount of MnO₂ could be easily modulated by the reaction time.

The XPS are conducted to study the surface states. The spectra of O 1s, Ti 2p, Mn 2p and Co 2p_{3/2} are displayed in Fig. 4, while the mole ratios of concentration about different elemental oxidation states are summarized in Table 2. As depicted in Fig. 4a, the O 1s bands over these three catalysts can be

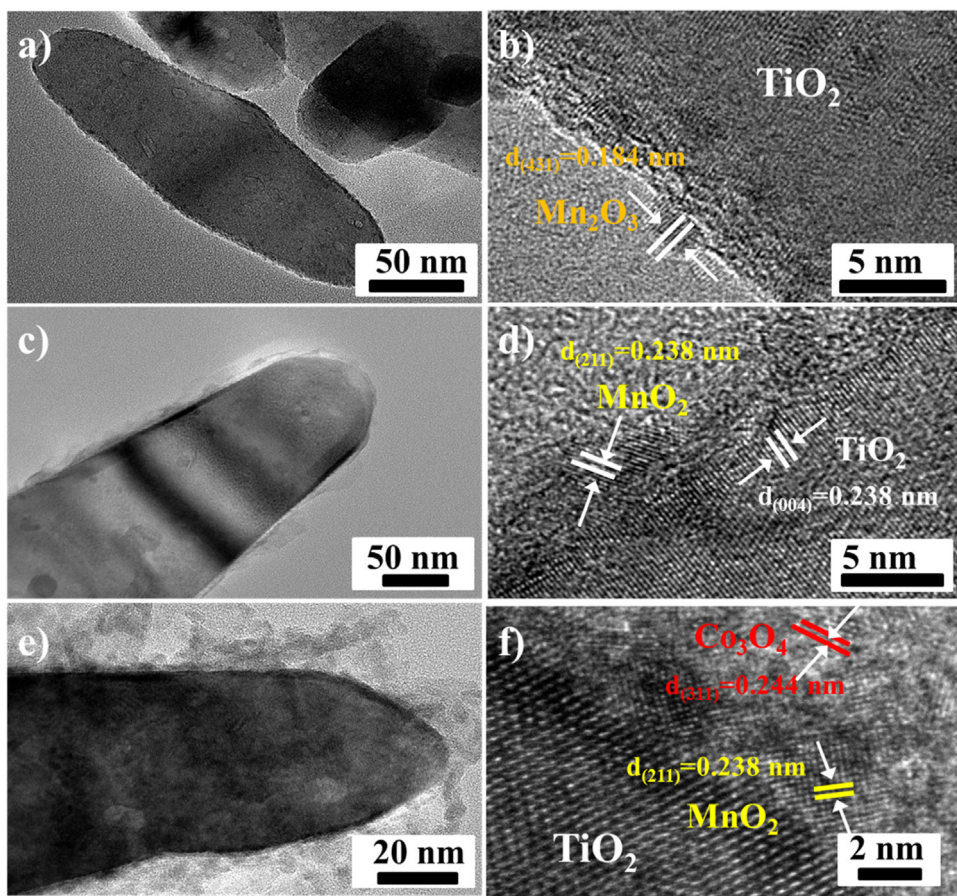


Fig. 2. The HRTEM images of different samples: (a,b) Mn/TiO₂-I; (c,d) Mn/TiO₂-P; (e,f) Mn-Co/TiO₂-P.

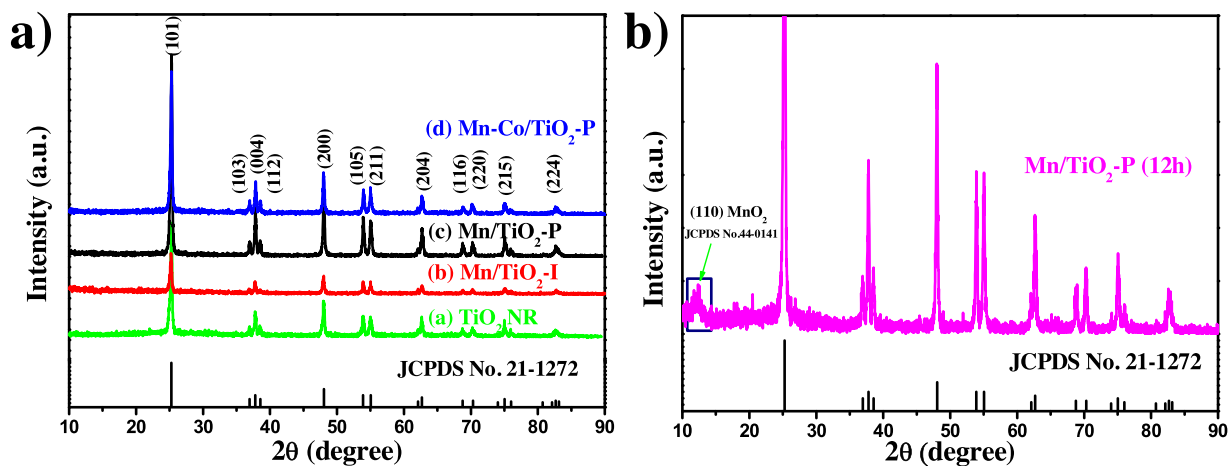


Fig. 3. X-ray diffraction patterns of (a) different samples and (b) Mn/TiO₂-P (12 h).

Table 2

The relative concentration ratios of Mn, Co and O for different samples.

Samples	Relative concentration ratios (%)		
	Mn ⁴⁺ /Mn	Co ³⁺ /Co	O _a /O
Mn/TiO ₂ -I	35.64	–	42.05
Mn/TiO ₂ -P	44.56	–	58.18
Mn-Co/TiO ₂ -P	55.34	69.39	60.39

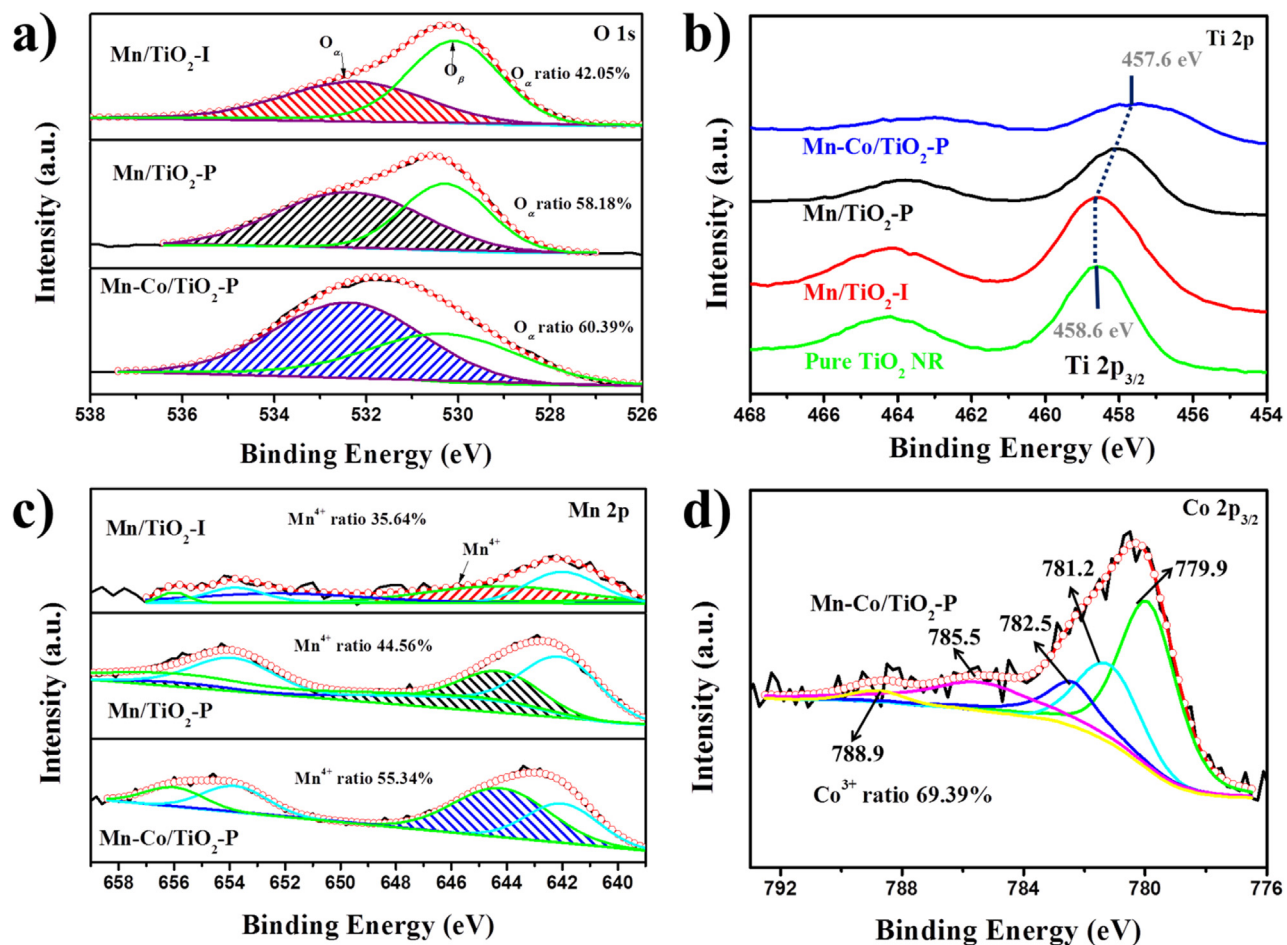


Fig. 4. XPS spectra for O 1s (a), Ti 2p (b), Mn 2p (c) and Co 2p_{3/2} (d) of the different samples.

fitted into two peaks, corresponding to the surface adsorbed oxygen from the oxide defects or hydroxyl groups (denoted as O_α) at 531.6–532.0 eV and lattice oxygen (denoted as O_β) at 529.6–530.2 eV, respectively [31]. The relative concentration percentages of O_α /O increased in the following sequence: Mn/TiO₂-I (42.05%) < Mn/TiO₂-P (58.18%) < Mn-Co/TiO₂-P (60.39%). Generally, surface adsorbed oxygen is believed to be responsible for high activity than lattice oxygen ascribed to its high mobility and strong NO oxidation ability, which facilitated the “Fast SCR” process [32]. Hence, the photocatalytic method exhibited the advantage in the preparation of the highly effective NH₃-SCR catalysts.

The Ti 2p spectra are shown in Fig. 4b. The peaks at 458.5 and 464.2 eV in the pure TiO₂ NRs, which are characteristic of the Ti⁴⁺ species [33], are assigned to Ti 2p_{3/2} and Ti 2p_{1/2}, respectively. As for Mn/TiO₂-I, its binding energies (BEs) are close to the pure TiO₂ NR, indicating the weak interaction between the TiO₂ support and MnO₂ active species [34], which agreed well with our results of H₂-TPR. However, Mn/TiO₂-P revealed a shift to lower BE compared with pure TiO₂, implying the formation of Ti³⁺ on the surface [35]. With the introduction of Co, the BE of Mn-Co/TiO₂-P continually shift to a much lower BE, suggesting the increase of Ti³⁺ species. Above results indicate that the Ti³⁺ species are prone to form when photocatalytic method was applied, which was probably due to the accumulation of photogenerated electrons in TiO₂ ($Ti^{4+} + e^- (TiO_2) \rightarrow Ti^{3+}$) [36,37]. To prove this speculation, we conducted the photocatalytic process of Mn-Co/TiO₂-P preparation without the participation of light in the second stage. We did find out that the position of Ti 2p didn't shift to lower BE compared

with that of Mn/TiO₂-P (Fig. S4a). Therefore, it could be concluded that the photocatalytic process is beneficial to the formation of Ti³⁺. The high reducible Ti³⁺ species has been reported to be important in NH₃-SCR reaction due to the formation and transfer of lattice oxygen [38,39].

Two distinct peaks centered at 642.0 and 653.8 eV were observed and ascribed to Mn 2p_{3/2} and Mn 2p_{1/2}, respectively (Fig. 4c) [27]. The intensities of XPS peaks via photocatalytic reaction became stronger due to more Mn⁴⁺ intimately interaction with TiO₂ support surface and also more electronic transfer between MnO₂ active component and TiO₂ support [40]. By peak-fitting deconvolutions, the Mn 2p_{3/2} spectra can be reasonably divided into three characteristic sub-peaks assigned to Mn²⁺ (640.4 eV), Mn³⁺ (642.0 eV) and Mn⁴⁺ (644.2 eV), respectively [41]. As listed in Table 2, Mn⁴⁺/Mn molar ratio for Mn/TiO₂-P (44.56%) and Mn-Co/TiO₂-P (55.34%) are higher in contrast to the counterparts via impregnation (35.64%), which demonstrates the photocatalytic method and the further introduction of Co species are beneficial to the formation of Mn⁴⁺. This result is accordant with the HRTEM and XRD results. The spectra of Co 2p_{3/2} can split into five peaks (Fig. 4d), which is consistent with the reports previously [42]. The relative concentration ratio of Co³⁺/Co in Mn-Co/TiO₂-P is about 69.39%, which is approximate to the stoichiometric value of Co₃O₄ (66.67%).

On the basis of the above results and discussion, it can be concluded that the flocculent and open nanostructured MnO₂ and Co₃O₄ could be closely loaded over TiO₂ by photocatalytic reaction. The MnO₂-(Co₃O₄)/TiO₂ hybrids could provide MnO₂ species,

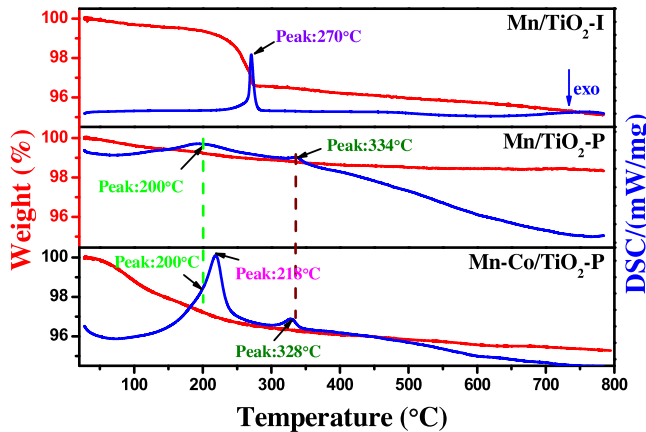


Fig. 5. TGA and DSC curves of different samples in air with a heating speed of $10\text{ }^{\circ}\text{C min}^{-1}$.

more surface active oxygen and more existence of surface Ti^{3+} , thus contributing to improve the $\text{NH}_3\text{-SCR}$ activity.

3.2. The formation of $\text{Mn/TiO}_2\text{-P}$ and $\text{Mn-Co/TiO}_2\text{-P}$ nanostructures

To understand the formation mechanism of $\text{Mn/TiO}_2\text{-P}$ and $\text{Mn-Co/TiO}_2\text{-P}$ nanostructures, a series of experiments were performed. Firstly, we observed that KMnO_4 was hard to react with TiO_2 NRs in the absence of light (Table S2, Entry 1), indicating that the participation of light is a prerequisite to constructing the nanostructures. Secondly, the influences of irradiation durations (a, 0 min; b, 15 min; c, 1 h; d 2 h; e, 4 h; f, 8 h) on the morphologies of Mn/TiO_2 was also studied as shown in Fig. S1. It was obvious that the thickness of the flocculent MnO_2 increased with the increase of irradiation duration. The corresponding surface specific areas were also gradually increased, as proved in Table S3 and Fig. S5. These observations imply that the thickness of flocculent MnO_2 could be easily tuned to a large extent by varying the irradiation duration, further confirming the importance of irradiation. According to the previous literatures, the potential of TiO_2 conduction band was $\sim -0.20\text{ V}$ (vs NHE) while the redox potential of the couple $\text{MnO}_4^-/\text{MnO}_2$ was $+1.69\text{ V}$ (vs NHE), thus suggesting the Eq. (1) was prone to happen [43]. The MnO_2 might also be formed by the decomposition of KMnO_4 via photolysis and auto-catalysis (Eq. (2)) [44].

When Co was introduced, the pH value was found immediately decreased, indicating the rapid consumption of OH^- ions. It could be deduced that cobalt hydroxides might be formed during this process. TGA in air was employed to confirm the speculation, as presented in Fig. 5. As for $\text{Mn/TiO}_2\text{-P}$, there are two peaks located at 200 and $334\text{ }^{\circ}\text{C}$. The former peak was ascribed to the evaporation of absorbed water. The weight percentage in TG was almost unchanged for latter, indicating further crystallization of MnO_2 . Strikingly, after the introduction of $\text{Co}(\text{NO}_3)_2\cdot 6\text{H}_2\text{O}$ in $\text{Mn/TiO}_2\text{-P}$ sample, it appears a new peak centered at $218\text{ }^{\circ}\text{C}$, which is mainly due to the decomposition of the intermediate Co species, namely cobalt hydroxides. Meanwhile, the weight loss in TG at $218\text{ }^{\circ}\text{C}$ was obvious and the endothermic peak was abrupt, further suggesting the procedure of dehydration. Additionally, to demonstrate the dehydration of Co species, we also directly loaded Co species onto the TiO_2 NRs via photocatalytic method. Similarly, the decomposition temperature of Co precursor for $\text{Co/TiO}_2\text{-P}$ was also approximate to that of $\text{Mn-Co/TiO}_2\text{-P}$ (Fig. S6) and previous reports [45]. As for $\text{Mn/TiO}_2\text{-I}$, the peak between 220 and $300\text{ }^{\circ}\text{C}$ is ascribed to the thermal decomposition of manganese acetate. The crystallographic structure of the cobalt hydroxides was further ana-

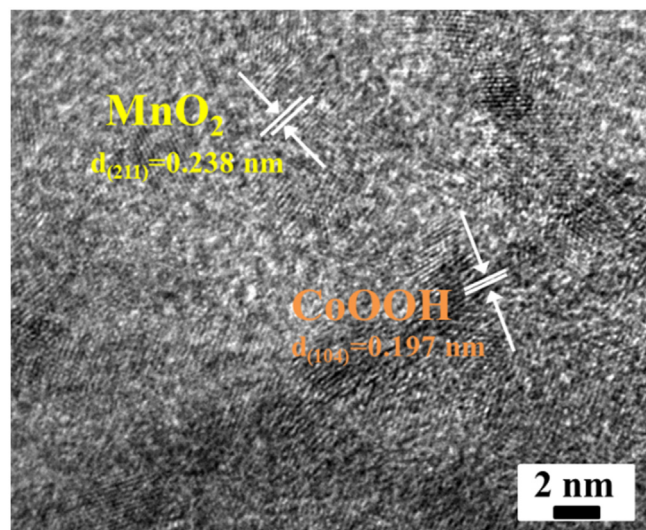


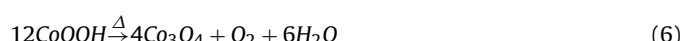
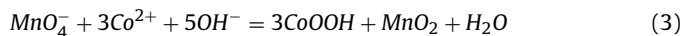
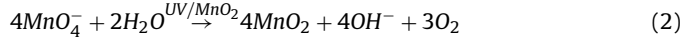
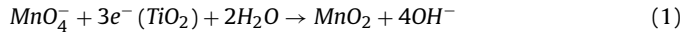
Fig. 6. The HRTEM image of the $\text{Mn-Co/TiO}_2\text{-P}$ before calcination.

lyzed by HRTEM technique. It was found that the lattice fringes are attributed to CoOOH (JCPDS No. 14-0673) before sintering (Fig. 6).

Above results demonstrated the formation of CoOOH with the introduction of Co^{2+} precursor. There are two possibilities for the oxidation of Co^{2+} to Co^{3+} . The first one is the direct redox reaction between Co^{2+} and KMnO_4 (Eq. (3)), which has been proved by other works [46]. The other one is the oxidation of Co^{2+} by photogenerated holes (Eq. (4)). To manifest the strong oxidation ability of photogenerated holes, we carried out the following experiment: Co^{2+} precursor and TiO_2 NRs in the absence of KMnO_4 solutions were both dispersed in NaIO_3 solution and exposed in the irradiation of UV light (Table S2, Entry 3). We did observe the new formation of nanoparticles. In theory, the potential of the valence band in TiO_2 was about $+2.7\text{ V}$ (vs NHE) [47], while the pair $\text{Co}^{2+}/\text{Co}^{3+}$ was -1.8 V (vs NHE), further suggesting that Co^{2+} is able to oxidized to Co^{3+} by the photogenerated holes. On the other hand, we also performed the process of $\text{Mn-Co/TiO}_2\text{-P}$ preparation without the irradiation in the second stage. The obtained sample was denoted as Mn-Co(dark)/TiO_2 . As shown in Table S2, the morphologies of Mn-Co(dark)/TiO_2 (Entry 4) was different from that of $\text{Mn-Co/TiO}_2\text{-P}$ (Entry 5). Some new formed nanostructures were dissociated from the TiO_2 NRs rather than solely anchored on the supports for $\text{Mn-Co/TiO}_2\text{-P}$. It was then deduced that the photogenerated holes dominated the oxidation of Co^{2+} for the formation of the $\text{MnO}_2\text{-Co}_3\text{O}_4$ shell/ TiO_2 core nanostructures.

As expected, the binding energy of $\text{Co/TiO}_2\text{-P}$ was decreased after calcination (Fig. S4b), indicating that the valence state of Co species was also decreased [48]. It is quite conceivable that cobalt nitrate was simultaneously oxidized to $+3$ valence by KMnO_4 and photogenerated holes, then completely converted to Co_3O_4 during calcination process (Eqs. (3–6)) [49]. All the involved experiments are sum up in Table S2.

Based on the above analysis, a formation mechanism was then proposed according to the below equations:



Initially, TiO_2 NRs were homogeneously dispersed in MnO_4^- solution. Driven by the UV light, photogenerated electrons and holes were separated and migrated to the surface for the followed redox reaction. Subsequently, flocculent MnO_2 were rapidly formed by the reduction of MnO_4^- by photoexcited electrons (Eq. (1)) and the decomposition of KMnO_4 via photolysis and autocatalysis (Eq. (2)). With the introduction of Co, $\text{Co}(\text{NO}_3)_2 \cdot 6\text{H}_2\text{O}$ was oxidized to Co^{3+} mainly by the photogenerated holes (Eq. (4)) rather than KMnO_4 (Eq. (3)). Co^{3+} then was rapidly and equally deposited over MnO_2 in the form of CoOOH (Eq. (5)). Finally, the intermediate CoOOH were completely converted to Co_3O_4 during calcination process (Eq. (6)), forming the $\text{MnO}_2\text{-Co}_3\text{O}_4$ hybrids with compact flocculent structures.

3.3. SCR performance

As mentioned above, the development of low temperature SCR catalysts is still a big challenge for the abatement of NO_x . The manganese oxides based catalyst and the hybrids of manganese oxides and cobalt oxides have been proved effective in the SCR reactions. This reaction then was chosen to explore the application of the novel nanostructured $\text{MnO}_2\text{-}(\text{Co}_3\text{O}_4)\text{/TiO}_2$. No doubt, we believe this new nanostructure of $\text{MnO}_2\text{-}(\text{Co}_3\text{O}_4)\text{/TiO}_2$ were also interested in other applications of environmental catalysis like CO oxidation, the oxidation of formaldehyde and so on.

For comparison, $\text{MnO}_2\text{/TiO}_2$ ($\text{Mn/TiO}_2\text{-I}$) was also prepared by a wetness impregnation method to study the SCR performance. The NO conversion with respect to the temperature range (90–350 °C) of the catalysts is shown in Fig. 7a. It was found out that the catalytic performance of $\text{Mn/TiO}_2\text{-I}$ was not good and the highest NO conversion at the temperature of 330 °C was about 65%. As for $\text{Mn/TiO}_2\text{-P}$ catalyst, it shows 85% conversion at 255 °C. What is more, the operating temperature windows were further remarkably shifted to lower temperature after the introduction of Co, which exhibits 92% conversion at 125 °C. In this case, it must be pointed out that the amount of Mn is less over $\text{Mn/TiO}_2\text{-I}$ than that over $\text{Mn/TiO}_2\text{-P}$. To exclude the influence of Mn amount, we further tested the activity of Mn/TiO_2 with less Mn amount (0.80% and 1.42%) by reducing the irradiation duration to 15 min and 1 h (Fig. S7). It was found out that a better SCR performance was obtained when the irradiation duration is reduced to 1 h, which illustrated that the more amount of flocculent MnO_2 is detrimental to the SCR activity. On the other hand, even though the Mn percentage via irradiation for 15 min (0.80%) is less than that on $\text{Mn/TiO}_2\text{-I}$ (1.65%), the corresponding activity is remarkably more than the latter. All the above results display that the $\text{Mn/TiO}_2\text{-P}$ by photocatalytic process noticeably promoted the low temperature $\text{NH}_3\text{-SCR}$ performance and broaden the operating temperature windows compared with $\text{Mn/TiO}_2\text{-I}$.

Besides, we also compared the catalytic performance of $\text{Mn/TiO}_2\text{-P}$ with the results from literatures. It was found out that the photocatalytic preparation did show some advantages over the catalytic performance. As shown in the following table S4, the low temperature of the working window could achieve as low as 120 °C, but the loading amounts of Mn were extraordinarily high which would remarkably increase the production costs. When the loading amount of Mn decreased to 5.21%, the low temperature (NO conversion >70%) of the working window achieve higher than 200 °C. Therefore, $\text{Mn/TiO}_2\text{-P}$ in this work could well balance both the loading amount of Mn and the catalytic performance. Furthermore, the catalytic performance of $\text{Mn/TiO}_2\text{-P}$ could be further promoted with the introduction of Co species [50–52].

Furthermore, the introduction of Co could further achieve the enhanced SCR performance at low temperature. The N_2 selectivity was shown in Fig. 7b. It was found out that the performance for the pure $\text{MnO}_2\text{/TiO}_2$ hybrids including both $\text{Mn/TiO}_2\text{-I}$ and $\text{Mn/TiO}_2\text{-P}$ were not good due to the formation of N_2O by the bypass reaction.

Fortunately, the N_2 selectivity was significantly promoted to some extent with the introduction of Co species, indicating that the introduced Co could restrain the bypass reaction. Besides, we prepared the Mn-Co/TiO_2 samples by an incipient wetness impregnation method as a reference catalyst. It was found out that $\text{Mn-Co/TiO}_2\text{-P}$ showed superior low-temperature SCR performance compared to the $\text{Mn-Co/TiO}_2\text{-I}$ catalysts (Fig. S10). Thus, the photocatalytic method was proved to be an effective way to prepare $\text{Mn-Co/TiO}_2\text{-P}$ with very good SCR catalytic performance.

Since the $\text{Mn-Co/TiO}_2\text{-P}$ possess the best SCR performance, we further investigated the stability and H_2O durability as the target catalyst. Fig. 7c shows the long term stability of NO_x reduction over $\text{Mn-Co/TiO}_2\text{-P}$. It exhibits strong thermal stability with essentially no deactivation during at least 72 h. After SCR reaction, there is no pronounced variation and collapse in the morphology of the catalysts for $\text{Mn-Co/TiO}_2\text{-P}$ than fresh catalyst (Fig. S8). Since H_2O (2–15 vol.%) usually exists in the exhaust and has a strong effect on the performance of the catalysts, the H_2O durability then was further investigated by introducing 8 vol.% H_2O in the feed stream at 150 °C as shown in Fig. 7d. Inspiringly, the SCR activity was barely affected by 8 vol.% H_2O and exhibited an over 90% NO conversion during the test. Above results illustrated that the catalyst was robust and exhibited the good structural stability under catalytic conditions.

It is well-known that the surface acid sites and redox properties are of significance for the SCR reactions [53]. Then the $\text{NH}_3\text{-TPD}$ technique was employed to evaluate the surface acid situations (Fig. 8a). Generally, the low temperature peaks below 240 °C are assigned to NH_4^+ ions bound to the weak Brønsted (B) acid sites (denoted as weak acid sites), and the high temperature peaks between 250 and 500 °C are assigned to the strong Brønsted acid sites and the coordinated NH_3 originating from the Lewis (L) acid sites (collectively referred to strong acid sites) [54]. The area and position of the desorption peaks reflect the amounts and strength of acid sites, respectively [55]. Apparently, $\text{NH}_3\text{-TPD}$ plots of $\text{Mn/TiO}_2\text{-P}$ reveals the much broader areas at the whole temperature range than that of $\text{Mn/TiO}_2\text{-I}$, which indicated that there are much abundant and stronger of acid sites for $\text{Mn/TiO}_2\text{-P}$. With the introduction of Co, the low temperature desorption peaks of $\text{Mn-Co/TiO}_2\text{-P}$ further shift to the high temperature region and the area of desorption peaks become much larger.

The Py-IR was carried out to distinguish the B and L acid sites (Fig. S9). The Py-IR spectrum on all the samples shows characteristic bands at 1444 (very strong), 1572 (variable) and 1602 (strong) cm^{-1} due to pyridine molecule coordinately bonded to surface L acid sites, and displays bands at 1486 cm^{-1} (very strong), associated with both surface B and L acid sites [56,57]. The intensities of all the peaks for $\text{Mn/TiO}_2\text{-P}$ are obviously higher than $\text{Mn/TiO}_2\text{-I}$ no matter at 150 or 330 °C. The intensities become stronger with the introduction of Co species. Consequently, the samples obtained via photocatalytic reaction had more L and B acid sites which were favorable for SCR reactions.

To further identify the surface acid sites, the DRIFT spectra of NH_3 desorption at 30 °C among all the samples are carried out and the results are shown in Fig. 9a. The broad peaks centered at 1590–1610 and 1155–1185 cm^{-1} were assigned to asymmetric and symmetric bending vibrations of NH_3 coordinated with L acid sites, while the peaks at 1395–1410 cm^{-1} were ascribed to B acid sites [58]. It was evident that $\text{Mn/TiO}_2\text{-P}$ exhibited more both L and B acid species compared with $\text{Mn/TiO}_2\text{-I}$. Besides, the trend was more apparent with the introduction of Co species. The DRIFTS further reveal the catalyst via photocatalytic procedure possessed more stability L and B acid sites, which can further react with NO_x species to give harmless nitrogen at low temperature.

The redox properties of the catalysis were firstly evaluated by the $\text{H}_2\text{-TPR}$ (Fig. 8b). The feeble reduction peak centered at 428 °C can be associated with the reduction of Mn_2O_3 particles

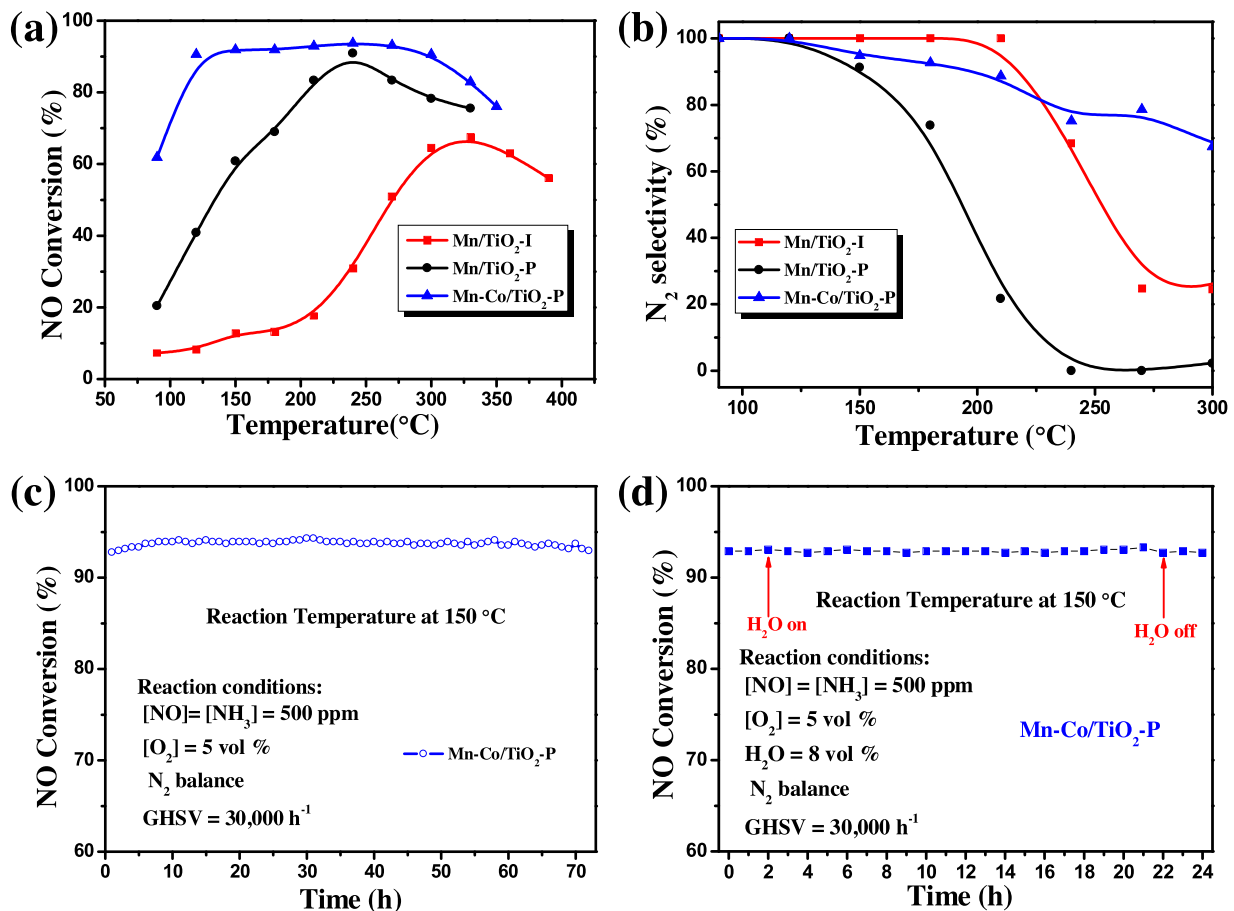


Fig. 7. NH₃-SCR performance (a) and N₂ selectivity (b) of different samples as a function of temperature, stability test (c) and H₂O durability test (d) of Mn-Co/TiO₂-P at 150 °C. Reaction conditions: [NO]=[NH₃]=500 ppm, [O₂]=5 vol %, H₂O=8 vol % (when used), N₂ balance, and GHSV=30,000 h⁻¹.

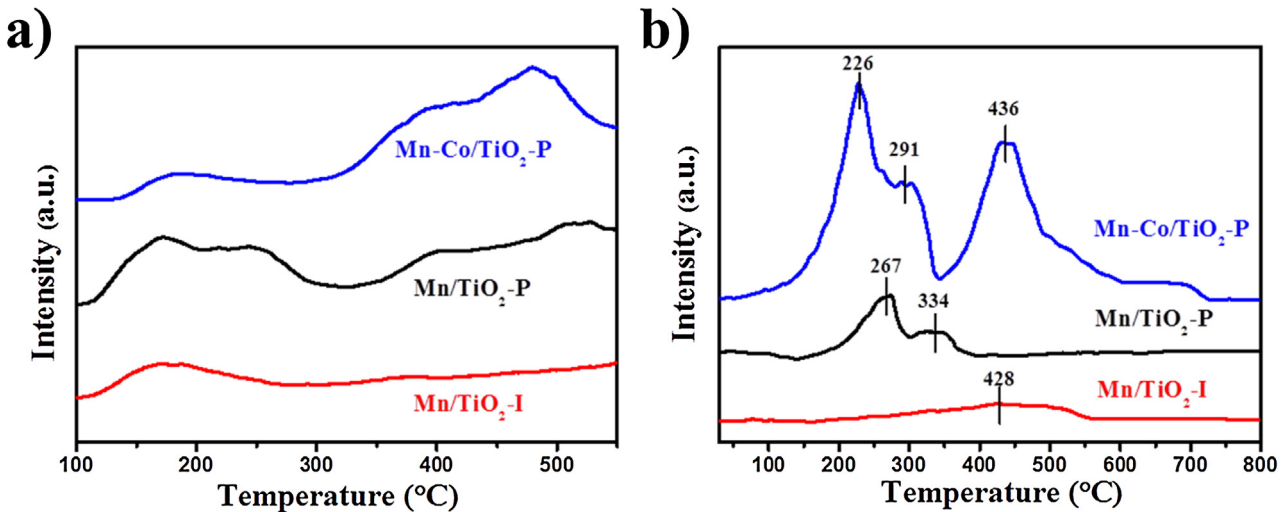


Fig. 8. NH₃-TPD profiles (a) and H₂-TPR profiles (b) of different samples.

having very slight interaction with the TiO₂ NR for the Mn/TiO₂-I. As for Mn/TiO₂-P, two distinct reduction peaks are observed at 267 and 334°C, which correspond to the two step reductions of Mn⁴⁺→Mn³⁺ and Mn³⁺→Mn²⁺ [59], further confirming that the dominant phase is MnO₂ instead of Mn₂O₃ for the Mn/TiO₂-P. The reduction peaks of manganese species is significantly shifted to much lower temperature as compared to that by impregnation

technique from 428 to 267°C. It has been reported that the Mn⁴⁺ is significant in the SCR reaction due to the high oxidation capability [60]. Furthermore, with the addition of Co ions, three broad and shark reduction profile peaks appeared at 226, 291 and 436°C, which was due to the reduction of both manganese and cobalt species. The intensities of all the peaks were obviously increased compared with that of both Mn/TiO₂-P and Mn/TiO₂-I. The peaks

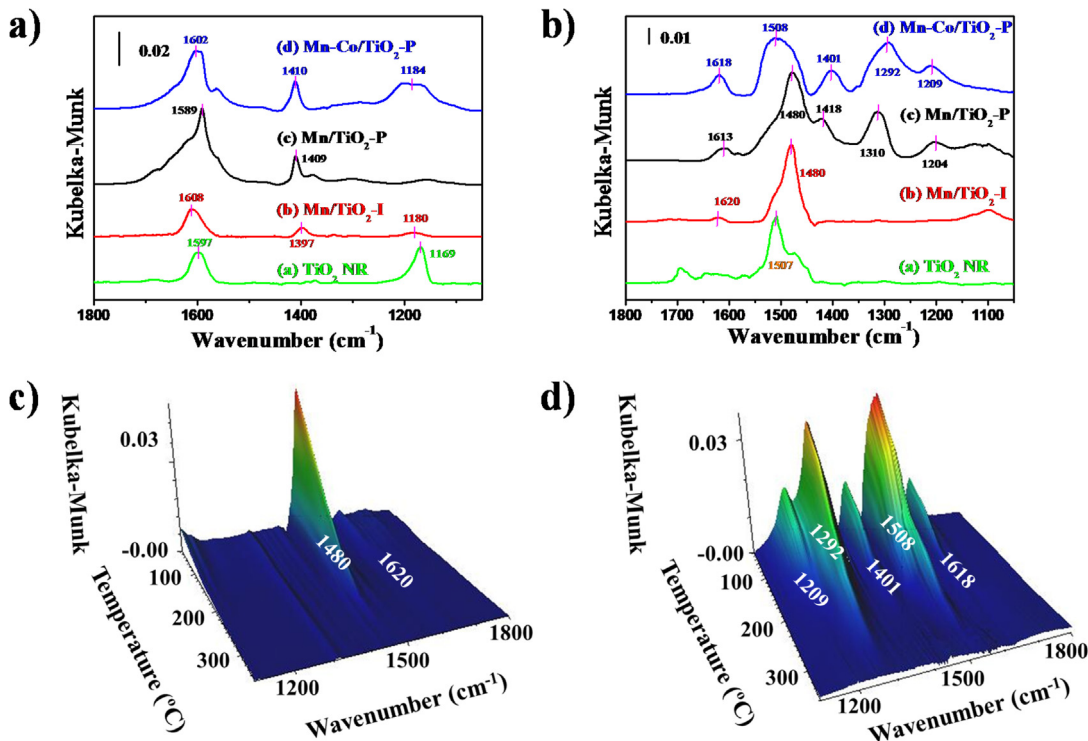


Fig. 9. In situ DRIFT spectra of NH_3 desorption on different samples at 30°C after the catalysts were exposed to a flow of 500 ppm of NH_3 for 1 h (a). In situ DRIFT spectra of NO_x desorption on different samples at 30°C (b) and on $\text{Mn}/\text{TiO}_2\text{-I}$ (c) and $\text{Mn}/\text{Co}/\text{TiO}_2\text{-P}$ (d) as a function of temperature after the catalysts were exposed to a flow of 500 ppm of $\text{NO} + 5\%$ O_2 for 1 h.

at 267 and 334°C corresponding to the reduction of MnO_2 were further shifted toward a lower temperature to 226 and 291°C , respectively. The reduction peak at 436°C with an apparent shoulder in a higher temperature could be interpreted as a stepwise reduction of Co^{3+} to Co^{2+} and CoO to metallic cobalt [61]. Benefited from the existence of more Mn^{4+} species and the introduction of Co species, the materials prepared via photocatalytic method exhibit promoted redox property which was significant in NH_3 -SCR reaction [62].

In situ DRIFT spectra of $\text{NO} + \text{O}_2$ co-adsorption at 30°C was performed to estimate the adsorption behavior of surface NO_x species (Fig. 9b). As for $\text{Mn}/\text{TiO}_2\text{-I}$, a new and very weak peak appeared at 1620 cm^{-1} (gaseous NO_2) compared with that of pure TiO_2 [63]. With respect to $\text{Mn}/\text{TiO}_2\text{-P}$, the intensity of the peak at $\sim 1613\text{ cm}^{-1}$ was obviously increased. Besides, several distinct new peaks emerged at ~ 1418 ($\text{trans-N}_2\text{O}_2^{2-}$) [64,65], ~ 1310 (monodentate nitrites) [41] and $\sim 1204\text{ cm}^{-1}$ (chelating nitrites) [66]. Along with the introduction of Co species, the spectra were quite similar with that of $\text{Mn}/\text{TiO}_2\text{-P}$. However, the intensity of the peak at $\sim 1613\text{ cm}^{-1}$ was further increased compared with that of $\text{Mn}/\text{TiO}_2\text{-P}$. The peak at $\sim 1310\text{ cm}^{-1}$ shifted to the lower wavenumber centered at 1292 cm^{-1} [67], illustrating the transform of monodentate nitrites to monodentate nitrate. The spectra of NO_x desorption on $\text{Mn}/\text{TiO}_2\text{-I}$ and $\text{Mn}/\text{Co}/\text{TiO}_2\text{-P}$ as a function of temperature were shown in Fig. 9c and d, respectively. It was observed that the peaks at $\sim 1613\text{ cm}^{-1}$ could be observed at higher temperature over $\text{Mn}/\text{Co}/\text{TiO}_2\text{-P}$ compared with $\text{Mn}/\text{TiO}_2\text{-I}$, illustrating that the gaseous NO_2 was much stable over $\text{Mn}/\text{Co}/\text{TiO}_2\text{-P}$. On the other hand, the peaks at 1508 (monodentate nitrate) [68] and 1292 cm^{-1} always exist until 250°C on $\text{Mn}/\text{Co}/\text{TiO}_2\text{-P}$, suggesting the stronger adsorption behavior of NO_x species.

Above results showed that the samples prepared via photocatalytic method could provide much more NO_x species adsorbed on the surface both in category and quantity compared with that

of $\text{Mn}/\text{TiO}_2\text{-I}$. In those NO_x species, the gaseous NO_2 was widely accepted as a “Fast SCR” reaction intermediate could contribute to the SCR activity at low temperature [41]. The monodentate nitrate was helpful to the SCR reactivity at low temperature [69,70]. While the $\text{trans-N}_2\text{O}_2^{2-}$ and chelating nitrites were considered to be a candidate for an active intermediate in SCR reaction [71,72]. Therefore, NO could be much easier to be activated over the samples prepared via photocatalytic method than over pristine TiO_2 and $\text{Mn}/\text{TiO}_2\text{-I}$, which is possibly due to the abundant MnO_2 species, surface active oxygen and surface Ti^{3+} .

4. Conclusions

In summary, the $\text{MnO}_2\text{-(Co}_3\text{O}_4\text{)}/\text{TiO}_2$ hybrids with uniform flocculent shell/core nanostructure have successfully been constructed via photocatalytic method combined with the followed calcination process. Both Mn and Co were homogeneously distributed over the whole frameworks. The flocculent MnO_2 were in-situ formed on the backbone of TiO_2 NR through the reduction of MnO_4^- by photoexcited electrons and the decomposition of KMnO_4 via photolysis and auto-catalysis. Three steps were involved in the formation of $\text{MnO}_2\text{-Co}_3\text{O}_4$ hybrids, namely the oxidation of Co^{2+} to Co^{3+} by the photogenerated holes, the deposition of intermediate CoOOH over MnO_2 and finally the conversion of CoOOH to Co_3O_4 during calcination process. Both $\text{Mn}/\text{Co}/\text{TiO}_2\text{-P}$ and $\text{Mn}/\text{TiO}_2\text{-P}$ exhibited promoted SCR de NO_x performance compared with that of $\text{Mn}/\text{TiO}_2\text{-I}$, especially at the temperature below 255°C . Beyond the unique structural features, the samples prepared via photocatalytic method have abundant MnO_2 species, surface active oxygen and surface Ti^{3+} which are possibly contributed to the activation of NO_x , which is a key factor in SCR reaction. Besides, the improved amount and strength of the surface acid sites is also beneficial to the SCR reaction. We believe that the $\text{MnO}_2\text{-(Co}_3\text{O}_4\text{)}/\text{TiO}_2$ hybrids were also interested in other applications of environmental catalysis.

sis and the developed photocatalytic methods could be applied for preparing other functional nanostructures.

Acknowledgements

This work was financially supported by the National Natural Science Foundation of China (21303099) and the National Basic Research Program of China (973 Program, 2014CB660803).

Appendix A. Supplementary data

Supplementary data associated with this article can be found, in the online version, at <http://dx.doi.org/10.1016/j.apcatb.2016.10.071>.

References

- [1] H. Li, Z. Bian, J. Zhu, D. Zhang, G. Li, Y. Huo, H. Li, Y. Lu, *J. Am. Chem. Soc.* 129 (2007) 8406–8407.
- [2] T. Kamegawa, Y. Shimizu, H. Yamashita, *Adv. Mater.* 24 (2012) 3697–3700.
- [3] Z. Lin, X. Wang, *Angew. Chem. Int. Ed.* 52 (2013) 1735–1738.
- [4] K. Honda, A. Fujishima, *Nature* 238 (1972) 37–38.
- [5] R. Li, F. Zhang, D. Wang, J. Yang, M. Li, J. Zhu, X. Zhou, H. Han, C. Li, *Nat. Commun.* 4 (2013) 1432.
- [6] J. Zhang, Y. Wu, M. Xing, S.A.K. Leghari, S. Sajjad, *Energy Environ. Sci.* 3 (2010) 715–726.
- [7] C. Li, J. Yuan, B. Han, L. Jiang, W. Shangguan, *Int. J. Hydrogen Energy* 35 (2010) 7073–7079.
- [8] K.K. Sakimoto, A.B. Wong, P. Yang, *Science* 351 (2016) 74–77.
- [9] C. Chen, W. Ma, J. Zhao, *Chem. Soc. Rev.* 39 (2010) 4206–4219.
- [10] C. Pan, Y. Zhu, *Environ. Sci. Technol.* 44 (2010) 5570–5574.
- [11] C. Dai, J.M.R. Narayanan, C.R.J. Stephenson, *Nat. Chem.* 3 (2011) 140–145.
- [12] I. Ghosh, T. Ghosh, J.I. Bardagi, B. Konig, *Science* 346 (2014) 725–728.
- [13] J.C. Theriot, C.-H. Lim, H. Yang, M. Ryan, C.B. Musgrave, G.M. Miyake, *Science* 352 (2016) 1082–1086.
- [14] A.J. Bard, B. Kraeutler, *J. Am. Chem. Soc.* 100 (1978) 4317–4318.
- [15] N. Zhang, S. Liu, X. Fu, Y. Xu, *J. Phys. Chem. C* 115 (2011) 9136–9145.
- [16] C. Pacholski, A. Kornowski, H. Weller, *Angew. Chem. Int. Ed.* 43 (2004) 4774–4777.
- [17] T. Ohno, K. Sarukawa, M. Matsumura, *New J. Chem.* 26 (2002) 1167–1170.
- [18] L. Zhang, W. Wang, S. Sun, D. Jiang, E. Gao, *Appl. Catal. B* 162 (2015) 470–474.
- [19] F. Bocuzzi, A. Chiorino, M. Manzoli, P. Lu, T. Akita, S. Ichikawa, M. Haruta, *J. Catal.* 202 (2001) 256–267.
- [20] C. Zhang, H. He, K.-I. Tanaka, *Appl. Catal. B* 65 (2006) 37–43.
- [21] M. Xue, L. Huang, J. Wang, Y. Wang, L. Gao, J. Zhu, Z. Zou, *Nanotechnology* 19 (2008) 185604.
- [22] L. Zhang, L. Shi, L. Huang, J. Zhang, R. Gao, D. Zhang, *ACS Catal.* 4 (2014) 1753–1763.
- [23] X. Xie, Y. Li, Z. Liu, M. Haruta, W.J. Shen, *Nature* 458 (2009) 746–749.
- [24] F. Liu, H. He, Y. Ding, C. Zhang, *Appl. Catal. B* 93 (2009) 194–204.
- [25] D.A. Peña, B.S. Upadate, P.G. Smirniotis, *J. Catal.* 221 (2004) 421–431.
- [26] C. Liu, J. Shi, C. Gao, C. Niu, *Appl. Catal. A* 522 (2016) 54–69.
- [27] B. Thirupathi, P.G. Smirniotis, *Appl. Catal. B* 110 (2011) 195–206.
- [28] J. Li, D. Xu, *Chem. Commun.* 46 (2010) 2301–2303.
- [29] Y. Liu, J. Xu, H. Li, S. Cai, H. Hu, C. Fang, L. Shi, D. Zhang, *J. Mater. Chem. A* 3 (2015) 11543–11553.
- [30] J. Li, J. Chen, R. Ke, C. Luo, J. Hao, *Catal. Commun.* 8 (2007) 1896–1900.
- [31] L. Chen, J. Li, M. Ge, *J. Chem. Eng.* (2011) 531–537.
- [32] W. Shan, F. Liu, H. He, X. Shi, C. Zhang, *Chem. Commun.* 47 (2011) 8046–8048.
- [33] X. Gao, Y. Jiang, Y. Zhong, Z. Luo, K. Cen, *J. Hazard. Mater.* 174 (2010) 734–739.
- [34] X. Yao, L. Zhang, L. Li, L. Liu, Y. Cao, X. Dong, F. Gao, Y. Deng, C. Tang, Z. Chen, L. Dong, Y. Chen, *Appl. Catal. B* 150–151 (2014) 315–329.
- [35] Y. Li, Q. Zhong, *J. Hazard. Mater.* 172 (2009) 635–640.
- [36] R.F. Howe, M. Gratzel, *J. Phys. Chem.* 89 (1985) 4495–4499.
- [37] P. Liu, Y. Zhao, R. Qin, S. Mo, G. Chen, L. Gu, D.M. Chevrier, P. Zhang, Q. Guo, D. Zang, B. Wu, G. Fu, N. Zheng, *Science* 352 (2016) 797–800.
- [38] Z. Liu, Y. Yi, J. Li, S.I. Woo, B. Wang, X. Cao, Z. Li, *Chem. Commun.* 49 (2013) 7726–7728.
- [39] P.W. Seo, S.P. Cho, S.H. Hong, S.C. Hong, *Appl. Catal. A* 380 (2010) 21–27.
- [40] P.R. Ettireddy, N. Ettireddy, S. Mamedov, P. Boolchand, P.G. Smirniotis, *Appl. Catal. B* 76 (2007) 123–134.
- [41] H. Hu, S. Cai, H. Li, L. Huang, L. Shi, D. Zhang, *ACS Catal.* 5 (2015) 6069–6077.
- [42] J. Yang, H. Liu, W.N. Martens, R.L. Frost, *J. Phys. Chem. C* 114 (2010) 111–119.
- [43] J. Ryu, S.H. Lee, D.H. Nam, C.B. Park, *Adv. Mater.* 23 (2011) 1883–1888.
- [44] X. Hu, L. Shi, D. Zhang, X. Zhao, L. Huang, *RSC Adv.* 6 (2016) 14192–14198.
- [45] M. Figlarz, *J. Mater. Sci.* 11 (1976) 2267–2270.
- [46] C. Kuo, W. Lan, C. Chen, *Nanoscale* 6 (2014) 334–341.
- [47] H. Lee, W. Choi, *Environ. Sci. Technol.* 36 (2002) 3872–3878.
- [48] J. Yang, T. Sasaki, *Chem. Mater.* 20 (2008) 2049–2056.
- [49] B. Geng, F. Zhan, C. Fang, N. Yu, *J. Mater. Chem.* 18 (2008) 4977–4984.
- [50] Z. Wu, B. Jiang, Y. Liu, H. Wang, R. Jin, *Environ. Sci. Technol.* 41 (2007) 5812–5817.
- [51] J. Yu, F. Guo, Y. Wang, J. Zhu, Y. Liu, F. Su, S. Gao, G. Xu, *Appl. Catal. B: Environ.* 95 (2010) 160–168.
- [52] B. Jiang, Y. Liu, Z. Wu, *J. Hazard. Mater.* 162 (2009) 1249–1254.
- [53] F. Eigenmann, M. Maciejewski, A. Baiker, *Appl. Catal. B* 62 (2006) 311–318.
- [54] X. Zhao, L. Huang, H. Li, H. Hu, X. Hu, L. Shi, D. Zhang, *Appl. Catal. B* 183 (2016) 269–281.
- [55] S. Cai, H. Hu, H. Li, L. Shi, D. Zhang, *Nanoscale* 8 (2016) 3588–3598.
- [56] E.P. Parry, *J. Catal.* 2 (1963) 371–379.
- [57] Y. Fan, H. Xiao, G. Shi, H. Liu, Y. Qian, T. Wang, G. Gong, X. Bao, *J. Catal.* 279 (2011) 27–35.
- [58] Z. Wu, Y. Liu, H. Wang, R. Jin, *Environ. Sci. Technol.* 41 (2007) 5812–5817.
- [59] K. Zhuang, J. Qiu, F. Tang, B. Xu, Y. Fan, *Phys. Chem. Chem. Phys.* 13 (2011) 4463–4469.
- [60] F. Liu, W. Shan, Z. Lian, L. Xie, W. Yang, H. He, *Catal. Sci. Technol.* 3 (2013) 2699–2707.
- [61] Z. Zhu, G. Lu, Z. Zhang, Y. Guo, Y. Guo, Y. Wang, *ACS Catal.* 3 (2013) 1154–1164.
- [62] B. Thirupathi, P.G. Smirniotis, *J. Catal.* 288 (2012) 74–83.
- [63] Z. Liu, S. Zhang, J. Li, L. Ma, *Appl. Catal. B* 144 (2014) 90–95.
- [64] L. Xu, X.-S. Li, M. Crocker, Z.-S. Zhang, A.-M. Zhu, C. Shi, *J. Mol. Catal. A: Chem.* 378 (2013) 82–90.
- [65] G. Qi, R.T. Yang, R. Chang, *Appl. Catal. B* 51 (2004) 93–106.
- [66] X. Wu, F. Lin, H. Xu, D. Weng, *Appl. Catal. B* 96 (2010) 101–109.
- [67] L. Chen, J. Li, M. Ge, *Environ. Sci. Technol.* 44 (2010) 9590–9596.
- [68] C. Liu, L. Chen, J. Li, L. Ma, H. Arandian, Y. Du, J. Xu, J. Hao, *Environ. Sci. Technol.* 46 (2012) 6182–6189.
- [69] F. Liu, H. He, *J. Phys. Chem. C* 114 (2010) 16929–16936.
- [70] B. Guan, H. Lin, L. Zhu, B. Tian, Z. Huang, *Chem. Eng. J.* 181–182 (2012) 307–322.
- [71] K.I. Hadjivanov, *Catal. Rev.* 42 (2000) 71–144.
- [72] P. Savva, A. Efstathiou, *J. Catal.* 257 (2008) 324–333.